Available online at www.sciencedirect.com
ScienceDirect
Trans. Nonferrous Met. Soc. China 35(2025) 1619−1633
Transactions of Nonferrous Metals Society of China
www.tnmsc.cn

Improving comprehensive performance of Cu−Sn−P−Ni−Si alloy through composition and heat treatment optimization

Guo-liang LI[1], Zi-di HANG[1], Shi-peng YUE[1], Zhong-kai GUO[2], Jin-chuan JIE[1,3], Ting-ju LI[1,3]

1. Key Laboratory of Solidification Control and Digital Preparation Technology (Liaoning Province), School of Materials Science and Engineering, Dalian University of Technology, Dalian 116024, China;
2. School of Opto-electronic Engineering, Zaozhuang University, Zaozhuang 277160, China;
3. Ningbo Institute of Dalian University of Technology, Ningbo 315000, China

Received 15 September 2023; accepted 28 March 2024

Abstract: To optimize the comprehensive properties of Ni−Si precipitation strengthened phosphor bronze, the impact of the Ni/Si mass ratio and heat treatment process on a Cu−8Sn−0.1P−1Ni−*x*Si alloy was explored. High resolution field emission scanning electron microscopy and transmission electron microscopy were used for microstructural characterization. The results indicate that the properties are influenced by the Ni/Si mass ratio, attributed to the formation of various second phases. Simultaneously, by influencing the diffusion rate, the microstructures and properties are influenced by the solid solution treatment. The strength is enhanced by precipitated nanoscale particles during the aging process by influencing the motion of dislocations. Ultimately, excellent comprehensive properties, including ultimate tensile strength, yield strength, and elongation of 866 MPa, 772 MPa, and 8.7%, respectively, are obtained in the Cu−8Sn−0.1P−1Ni−0.227Si alloy.

Key words: phosphor bronze; Ni/Si mass ratio; precipitation; solid solution; Cu−Sn−P−Ni−Si alloy

1 Introduction

Phosphor bronze alloy demonstrates exceptional properties, including high strength [1,2], excellent bendability [3], remarkable corrosion resistance [4], and full waste recyclability. These attributes make it an environmentally friendly and optimal copper alloy for various applications, particularly in electrical connectors [5,6]. Furthermore, as technologies such as artificial intelligence and big data continue to advance, the new generation of connector materials is expected to exhibit even higher levels of performance and properties [7−9].

Traditional phosphor bronze falls short of meeting the requirements of the new generation of connector materials, resulting in a surge of interest in high-tin phosphor bronze (above 10 wt.% Sn) in recent years [5]. However, the application of high-tin phosphor bronze is hindered by certain limitations, including high cost and brittleness, which restrict its widespread use [10,11]. Nanoparticles can provide excellent performance [12−15]. In a previous work [9], Ni−Si precipitation strengthened phosphor bronze was developed, and the initial determination for the optimal composition was Cu−8Sn−0.1P−1Ni−0.24Si (wt.%). In Cu−Ni−Si alloys, the optimal Ni/Si mass ratio is approximately 4.2:1, which corresponds to an atomic ratio of 2:1 for Ni/Si [16,17]. However, in the Cu−8Sn−0.1P−1Ni−0.24Si alloy, in addition to the formation of the Ni_2Si phase, some $Ni_{31}Si_{12}$ and Ni_5P_4 phases were also formed [9]. Therefore, the

Corresponding author: Jin-chuan JIE, Tel: +86-411-84706220, E-mail: jiejc@dlut.edu.cn
https://doi.org/10.1016/S1003-6326(25)66771-9

optimal Ni/Si mass ratio for the Cu−8Sn−0.1P−1Ni−0.24Si alloy is subject to change. To achieve the optimal performance, it is necessary to optimize the composition of the Cu−Sn−P−Ni−Si alloy.

Solid solution treatment (SST) is a key process in alloy processing [18], with the aim of dissolving the soluble phases into the matrix [19,20] and preparing for the subsequent aging treatment. For aluminum alloys [18−22] and nickel-based alloys [23,24], numerous studies have been conducted on the effects of the SST process on alloy properties. For bronze with varying tin (Sn) contents, effective SST typically occurred within temperatures range of 600−800 °C [5,25,26]. Nevertheless, a deeper understanding is needed regarding the effect of SST temperature on the properties of tin bronze alloys. The SST process is actually controlled by atomic diffusion, which is dependent on temperature [27,28]. Meanwhile, experimental findings indicate that an inappropriate STT temperature can induce brittleness in the Ni−Si strengthened phosphor bronze, leading to cracking during the rolling process. The formation of cracks is commonly attributed to factors such as segregation [29,30], the inherent brittleness of the matrix [31], and local inhomogeneity of the particles [32]. However, the correlation between the SST process and the brittleness or formation of cracks in the matrix has not been extensively investigated. Additionally, phosphor bronze is known to present challenges in hot working processes [30,33]. Therefore, it is necessary to investigate the impact of STT temperature on Ni−Si strengthened phosphor bronze. Furthermore, the impact of aging on the properties of traditional phosphor bronze and Ni−Si strengthened phosphor bronze is different. Typically, aging temperatures range from 200 to 400 °C, and rapid grain growth occurs when aging temperature exceeds 500 °C [34,35]. However, there is limited research on the effect of aging temperature on phosphor bronze. Therefore, investigating appropriate heat treatment processes is particularly crucial.

Based on the Cu−8Sn−0.1P−1Ni−0.24Si alloy, the Ni/Si mass ratio was initially modified in this work to investigate its impact on the properties. The optimal Ni/Si mass ratio of 4.4:1, corresponding to the composition of Cu−8Sn−0.1P−1Ni−0.227Si, was determined by comparing the properties. Then, experiments were conducted at various temperatures to examine the impact of SST and aging temperature on the microstructure and properties of the Cu−8Sn−0.1P−1Ni−0.227Si alloy. The heat treatment temperatures were determined based on previous research on tin bronze. Through these investigations, an appropriate heat treatment process was determined. In-depth development of the properties of Cu−Sn−P−Ni−Si alloys was achieved by optimizing both composition and the heat treatment process. The mechanisms behind the influence of the Ni/Si mass ratio, STT temperature, and aging temperature on the microstructure and properties of Ni−Si precipitation strengthened phosphor bronze were also analyzed. Furthermore, understanding the mechanism of the SST temperature on alloy plasticity also provides insights into the hot working of the Cu−Sn−P−Ni−Si alloy.

2 Experimental

2.1 Sample preparation

Ingots with various Ni/Si mass ratios were prepared using an intermediate frequency induction furnace. The compositions with varying Ni/Si mass ratios were designed based on the Cu−8Sn−0.1P−1Ni−0.24Si alloy, and the specific compositions are presented in Table 1. The raw materials employed included electrolytic copper plate (99.95 wt.%), pure industrial tin (99.95 wt.%), Cu−14wt.%P master alloy, electrolytic nickel plate (99.95 wt.%), and pure silicon block (99.95 wt.%). After the preparation of the ingots, sampling and processing were conducted following the procedures illustrated in Fig. 1.

2.2 Heat treatment and rolling

After the optimal composition was determined, experiments were carried out at different temperatures to explore the effect of STT temperature on the Cu−Sn−P−Ni−Si alloy. As shown in Fig. 1, the bulk samples were solid solution treated at different temperatures ranging from 650 to 800 °C in the muffle furnace. The sample was placed into the furnace after reaching the target temperature and held for 2 h before being taken out and then quenched in water at room temperature. After the SST, microstructure and tensile samples were machined from the bulk sample.

Table 1 Nominal and chemical compositions of ingots with different Ni/Si mass ratios (wt.%)

Nominal Ni/Si mass ratio	Nominal composition	Chemical composition					Chemical Ni/Si mass ratio
		Cu	Sn	P	Ni	Si	
3.0:1	Cu−8Sn−0.1P−1Ni−0.333Si	Bal.	7.69	0.174	1.00	0.337	2.97:1
4.0:1	Cu−8Sn−0.1P−1Ni−0.250Si	Bal.	7.68	0.169	1.01	0.251	4.02:1
4.2:1	Cu−8Sn−0.1P−1Ni−0.238Si	Bal.	7.68	0.166	1.01	0.240	4.21:1
4.3:1	Cu−8Sn−0.1P−1Ni−0.232Si	Bal.	7.67	0.177	1.01	0.232	4.35:1
4.4:1	Cu−8Sn−0.1P−1Ni−0.227Si	Bal.	7.75	0.168	1.01	0.230	4.39:1
4.5:1	Cu−8Sn−0.1P−1Ni−0.222Si	Bal.	7.65	0.171	1.01	0.215	4.70:1
5.0:1	Cu−8Sn−0.1P−1Ni−0.200Si	Bal.	7.71	0.173	1.01	0.192	5.26:1

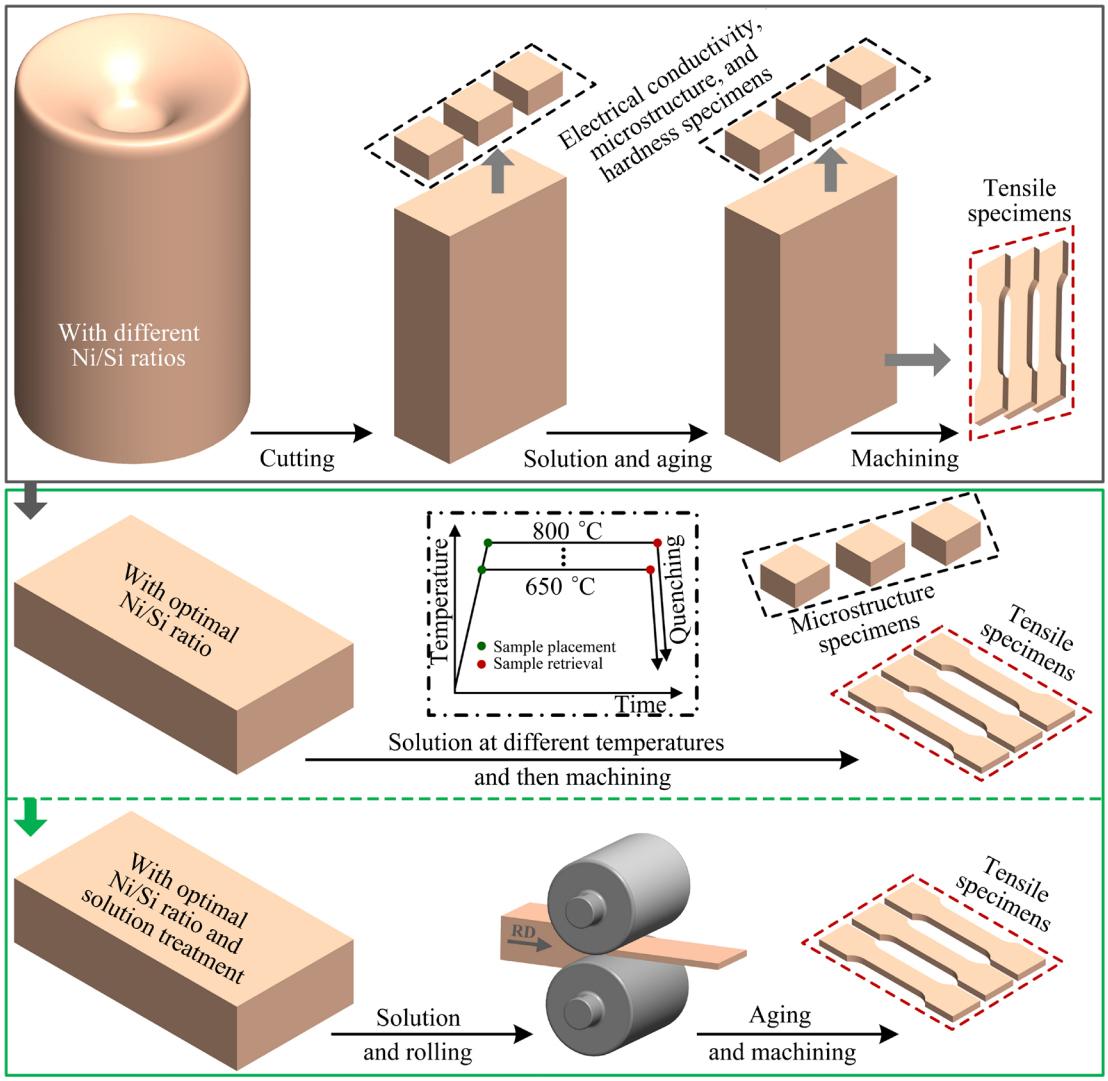

Fig. 1 Schematic diagram of sampling and experimental steps

After the optimal STT temperature was determined, cold rolling was performed on the Cu−Sn−P and Cu−Sn−P−Ni−Si bulk samples, followed by aging treatment at different temperatures to investigate the difference in properties between the two alloys.

2.3 Material characterization

The chemical compositions of the ingots were detected using X-ray fluorescence (XRF Shimadzu XRF−1800). X-ray diffraction (XRD) analysis was performed using a Bruker D8 Advance diffracto-meter equipped with a Cu radiation target. The

samples were polished and etched in a solution containing 95 mL C_2H_5OH + 5 mL HCl + 5 g $FeCl_3$. The microstructures were characterized by an optical metallographic microscope (OM) Olympus-GX51 and a high resolution field emission scanning electron microscopy (SEM) IT800-SHL. The microstructure was also characterized by transmission electron microscope (TEM) JEM− 2100F, and the TEM samples were prepared by twin-jet electro-polishing in a solution containing 30% HNO_3 and 70% CH_3OH at −30 °C.

The microhardness test was conducted using a Brinell hardness tester (HB−3000) with a load force of 306.25 N and a dwell time of 15 s. The electrical conductivity was measured using an electrical conductivity tester (Fischer-Sigmascope SMP 350). Tensile testing was carried out using a Suns-UTM5105 testing machine with a tensile rate of 1.0 mm/min. As shown in Fig. 1, the size of the samples for microstructure, electrical conductivity, and hardness measurement was 13 mm × 13 mm × 8 mm. The electrical conductivity and hardness test of each specimen were repeated at least seven times. The dog-bone-shaped tensile specimens with a gauge length of 20 mm, a width of 6 mm, and a thickness of 2 mm were sampled as shown in Fig. 1, and each tensile test was repeated at least three times.

3 Results

3.1 Effect of Ni/Si mass ratio on microstructure and properties of Cu−8Sn−0.1P−1Ni−*x*Si alloy

The as-cast OM microstructure of Cu−8Sn−0.1P−1Ni−*x*Si alloys with different Ni/Si mass ratios is shown in Figs. 2(a−g). The variation of the Ni/Si mass ratio has a relatively small effect on the as-cast microstructure, and all samples exhibit obvious dendritic morphology. As identified by the dotted line in Fig. 2(h), the interdendritic region consists of a eutectic microstructure composed of α-Cu and $Cu_{41}Sn_{11}$ phases [9]. Additionally, a small amount of rod-shaped $Ni_{31}Si_{12}$ phase, identified by the white arrows in Fig. 2(h), is randomly distributed in the matrix. After being solid solution treated at 700 °C for 2 h and aged at 400 °C for 4 h, the electrical conductivity and hardness of Cu−8Sn−0.1P−1Ni−*x*Si alloy with different Ni/Si mass ratios were tested under various conditions, as shown in Fig. 3. In the as-cast, solid solution, and aging states, an increasing trend in electrical conductivity is exhibited with the increase of the Ni/Si mass ratio, and a peak hardness is attained at the Ni/Si mass ratio of 4.4:1. The change in electrical conductivity is attributed to the decrease in total alloy content. Hence, the optimum Ni/Si mass ratio of the Cu−Sn−P−Ni−Si alloy is found at a ratio of 4.4:1.

Tensile testing was conducted on the alloys with various Ni/Si mass ratios after undergoing aging treatment, and the engineering stress−strain curves are shown in Fig. 4(a). From the engineering stress−strain curves, it is evident that only slight variations are observed in the strength of the alloys with different Ni/Si mass ratios, while significant differences are demonstrated in the elongation values. The values of ultimate tensile strength (UTS), yield strength (YS), and elongation (EL) of alloys with different Ni/Si ratios are shown in Fig. 4(b).

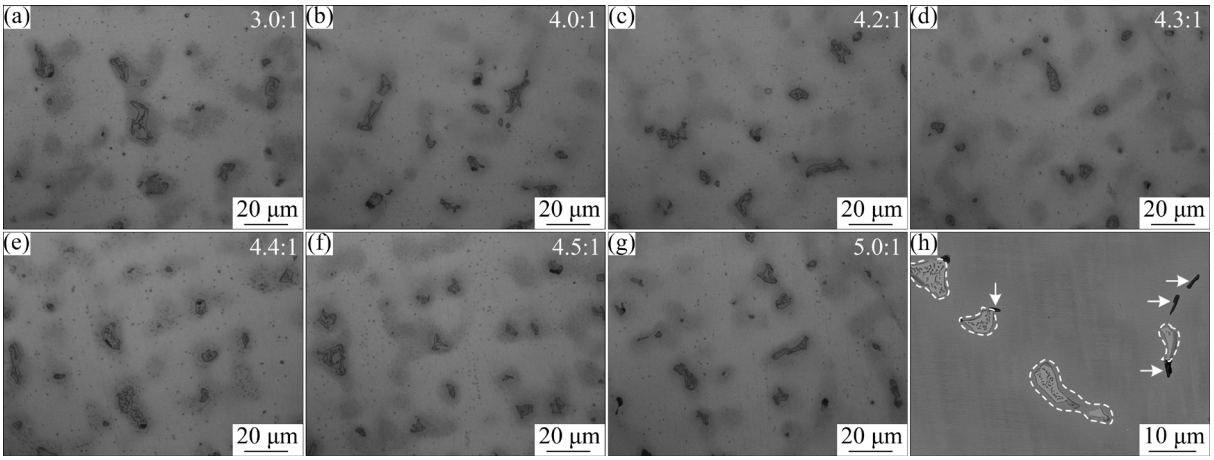

Fig. 2 (a−g) OM images of as-cast Cu−8Sn−0.1P−1Ni−*x*Si alloys with different Ni/Si mass ratios; (h) BSE image of eutectic microstructure and $Ni_{31}Si_{12}$ phase

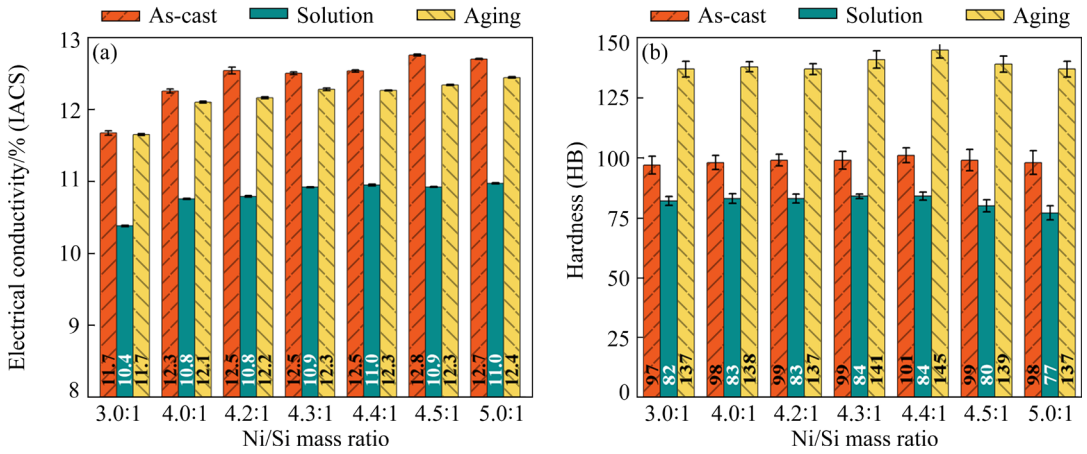

Fig. 3 Electrical conductivity (a), and hardness (b) of Cu−8Sn−0.1P−1Ni−*x*Si alloy with different Ni/Si mass ratios under different conditions

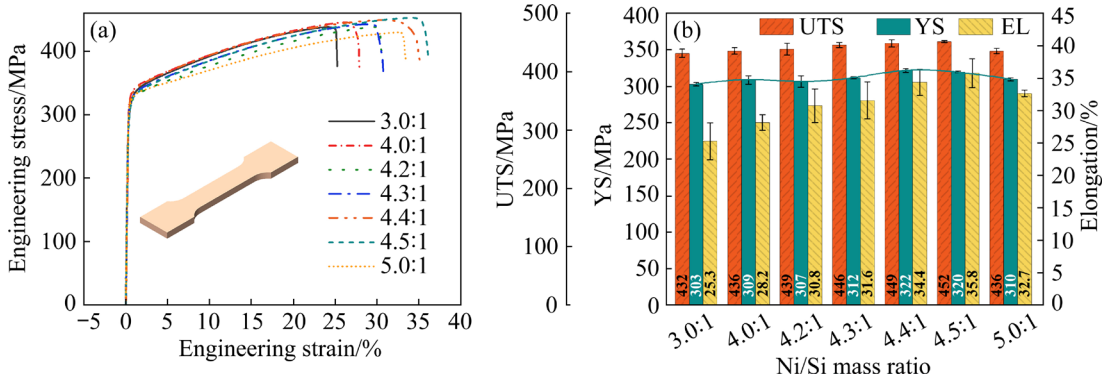

Fig. 4 Engineering stress−strain curves (a), and UTS, YS and EL (b) of aged samples with different Ni/Si mass ratios

With an increase in the Ni/Si mass ratio, UTS and YS exhibit slight fluctuations, and the YS reaches the maximum value when the Ni/Si mass ratio is 4.4:1. The EL significantly increases with increasing Ni/Si mass ratio, but it decreases when the Ni/Si mass ratio is 5:1. In summary, the Cu−8Sn−0.1P−1Ni−*x*Si alloy with a Ni/Si mass ratio of 4.4:1 exhibits the best comprehensive properties after SST and aging treatment. Therefore, the Cu−8Sn−0.1P−1Ni−0.227Si alloy presents good potential for practical applications.

3.2 Effect of STT temperature on microstructure and properties of Cu−8Sn−0.1P−1Ni−0.227Si alloy

To investigate the effect of STT temperature on the microstructure and properties of the Cu−8Sn−0.1P−1Ni−0.227Si alloy, a series of experiments were conducted at intervals of 10 °C from 650 to 800 °C. The SEM images of the Cu−8Sn−0.1P−1Ni−0.227Si alloy at representative SST temperatures are shown in Fig. 5. At low STT temperature, a large amount undissolved second phase particles are observed on the matrix (see Fig. 5(a)). The SEM images clearly show a significant decrease in the amount of undissolved second phase with the increase in STT temperature (see Fig. 5(b)). However, when the SST temperature exceeds 720 °C, the corrosion morphology of the grain boundary becomes more pronounced (see Figs. 5(d) and (e)). Moreover, as the SST temperature increases to 800 °C, wider and more pronounced corrosion morphology is observed, as shown in Fig. 5(f).

According to the characterization of microstructure, tensile tests were conducted on samples that underwent SST at 650, 700, 710, 720, 730, 740, 750, and 800 °C. As shown in Fig. 6, it can be observed that the properties of the alloy are relatively similar when the STT temperature is below 740 °C. However, when the STT temperature reaches 750 °C or even 800 °C, the EL and UTS of the alloy decrease significantly. As shown in Fig. 6(b), the UTS and YS gradually decrease as the STT

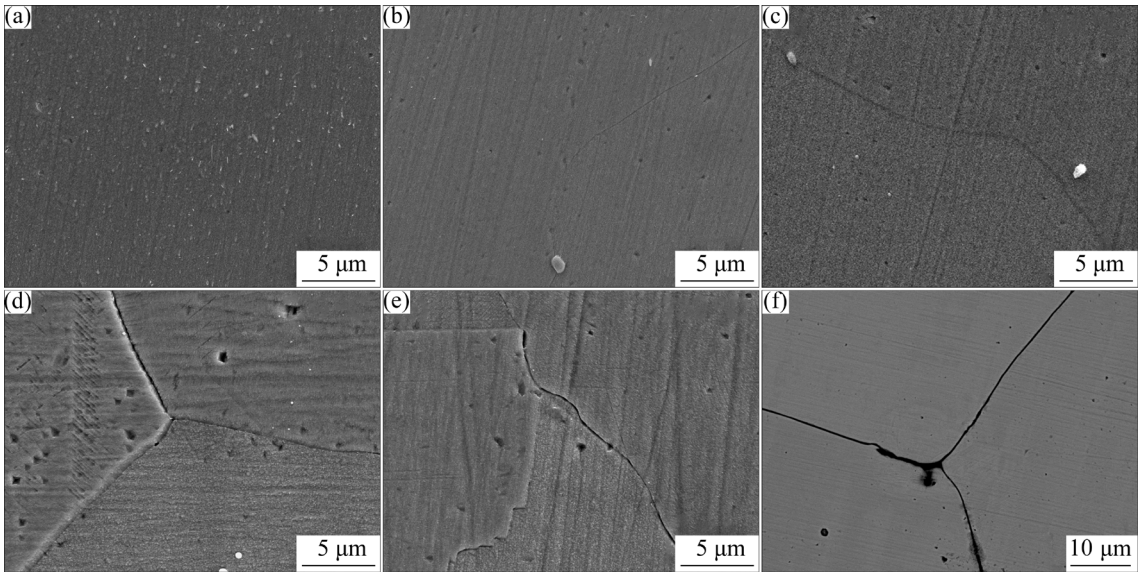

Fig. 5 SEM images of Cu−8Sn−0.1P−1Ni−0.227Si alloy after SST at different temperatures: (a) 650 °C; (b) 690 °C; (c) 710 °C; (d) 720 °C; (e) 730 °C; (f) 800 °C

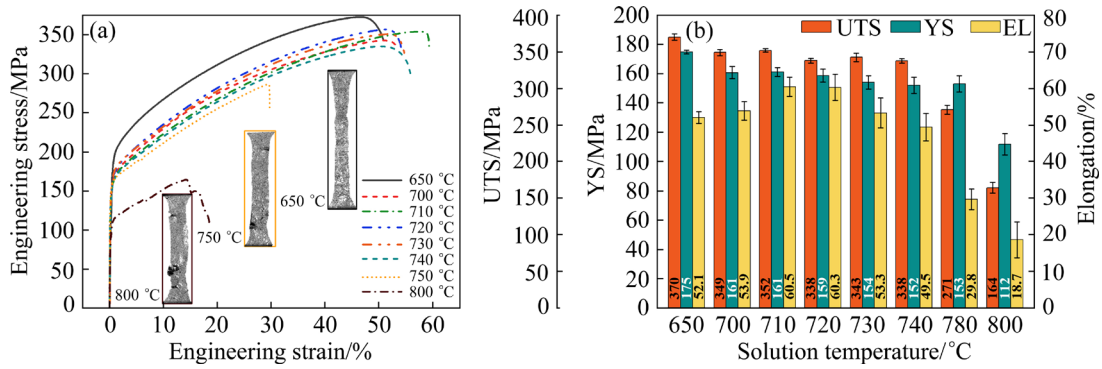

Fig. 6 Engineering stress−strain curves (a), and UTS, YS and EL (b) of aged samples at different STT temperatures for Cu−8Sn−0.1P−1Ni−0.227Si alloy

temperature increases. In contrast, the EL first increases and then decreases, reaching a peak value at 710 °C. The initial increase in EL is associated with the rise in solid solubility. However, the subsequent decrease in EL is closely related to grain boundary brittleness. Therefore, the ideal STT temperature for the Cu−8Sn−0.1P−1Ni−0.227Si alloy is determined to be 710 °C.

3.3 Effect of aging temperature on microstructure and properties of Cu−8Sn−0.1P−1Ni−0.227Si alloy

After SST at 710 °C for 2 h, Cu−8Sn−0.1P (S1) and Cu−8Sn−0.1P−1Ni−0.227Si (S2) alloys were cold-rolled by 80% (R80) and aged at different temperatures for 4 h. Tensile tests were performed on the aged samples, and the results are shown in Fig. 7. The strength values of the Cu−8Sn−0.1P and Cu−8Sn−0.1P−1Ni−0.227Si alloys are similar after being cold-rolled by 80%. However, as the aging temperature increases, the difference in strength between the Cu−8Sn−0.1P and Cu−8Sn−0.1P−1Ni−0.227Si alloys gradually increases. As shown in Fig. 7(d), with increasing aging temperature, the strength of the Cu−8Sn−0.1P alloy shows a decreasing trend. However, the strength of the Cu−8Sn−0.1P−1Ni−0.227Si alloy first decreases and then slightly increases. Excellent comprehensive properties of the Cu−8Sn−0.1P−1Ni−0.227Si alloy, with a UTS of 866 MPa, YS of 772 MPa, and EL of 8.7%, are achieved after 80% cold rolling followed by aging at 300 °C for 4 h. Certainly, when the aging temperature is raised to 400 °C, the Cu−8Sn−0.1P−1Ni− 0.227Si alloy also softens. This ultimately results in the Cu−8Sn−0.1P−1Ni−0.227Si alloy exhibiting good

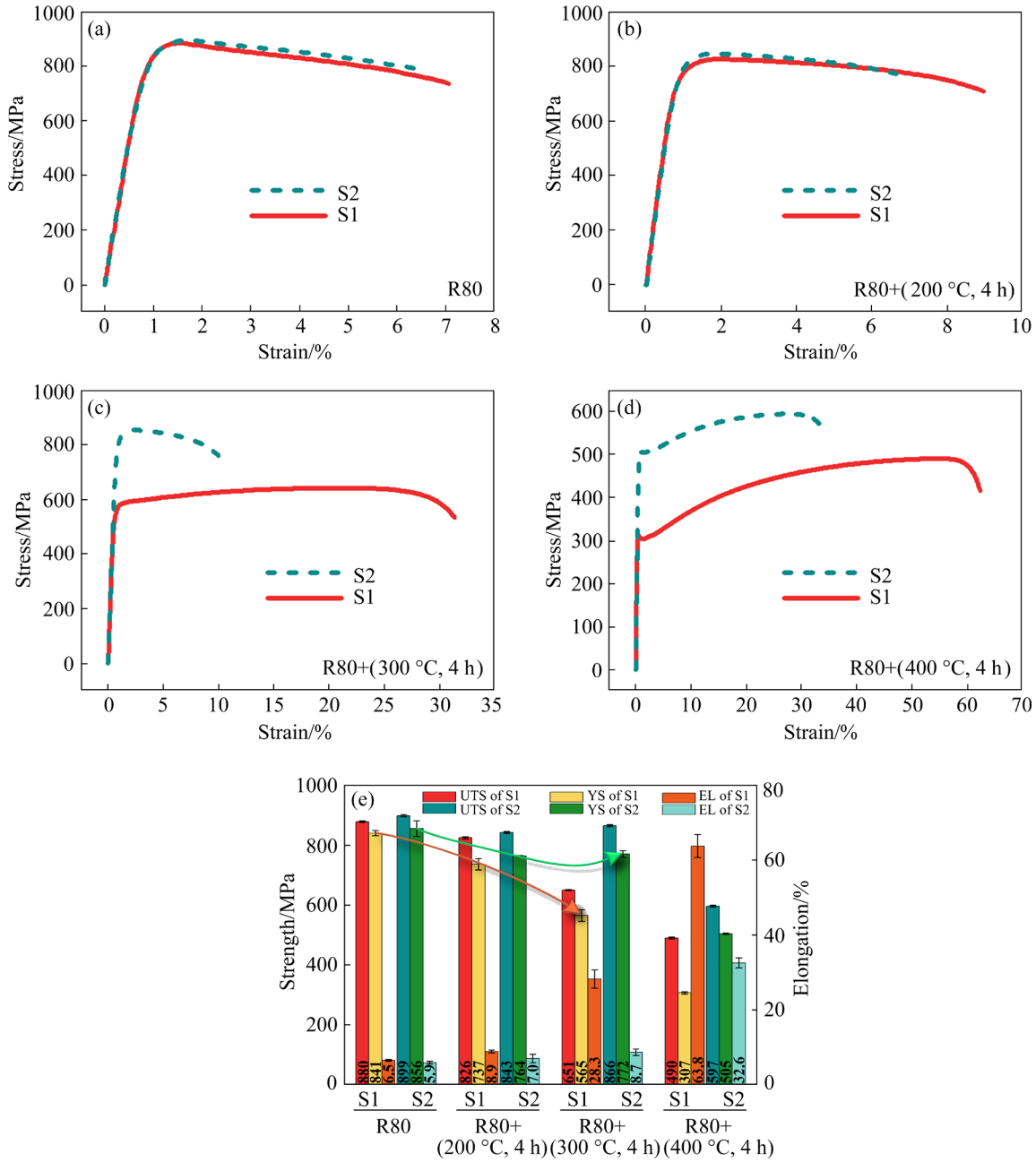

Fig. 7 Engineering stress−strain curves (a−d), and UTS, YS and EL (e) of cold-rolled samples and aged samples

comprehensive performance after aging at 300 °C. Additionally, better combination performance can be achieved by adding Ni and Si to the Cu−8Sn−0.1P alloy at higher temperatures. The durability and reliability of connectors fabricated with this alloy may be improved in industry.

4 Discussion

4.1 Optimal Ni/Si mass ratio of Cu−8Sn−0.1P−1Ni−*x*Si alloy

The presence of Ni_2Si nanoparticles precipitated after aging in the Cu−8Sn−0.1P− 1Ni−0.227Si alloy is revealed by TEM image in Fig. 8(a). The purpose of adding Ni and Si to the Cu−Sn−P alloy is to strengthen the alloy by forming the Ni_2Si phase in the matrix. Ideally, all added Ni and Si should contribute to the Ni_2Si phase, with a target Ni/Si mass ratio of 4.2:1 (atomic ratio 2:1) [16,17]. However, in the Cu−8Sn−0.1P−1Ni−*x*Si alloy, in addition to the Ni_2Si phase, the Ni_5P_4 and $Ni_{31}Si_{12}$ phases are also formed. Moreover, the electrical conductivity, hardness, strength, and elongation of the Cu−8Sn−0.1P−1Ni−*x*Si alloy are influenced by the Ni/Si mass ratio (see Figs. 3 and 4). Therefore, the analysis of the impact of the Ni/Si mass ratio on

this alloy is crucial for achieving optimal performance.

According to the metallographic images of the Cu−8Sn−0.1P−1Ni−*x*Si alloy in the solid solution state, the volume fraction of $Ni_{31}Si_{12}$ phases was statistically calculated, and then the mass fraction of $Ni_{31}Si_{12}$ phase was calculated via Eq. (1):

$$w(Ni_{31}Si_{12})=\varphi(Ni_{31}Si_{12})\frac{\rho_{Ni_{31}Si_{12}}}{\rho_{alloy}} \quad (1)$$

where $w(Ni_{31}Si_{12})$ is the mass fraction of $Ni_{31}Si_{12}$ phase, $\varphi(Ni_{31}Si_{12})$ is the volume fraction of $Ni_{31}Si_{12}$ phase, $\rho_{Ni_{31}Si_{12}}$ and ρ_{alloy} are the densities of $Ni_{31}Si_{12}$ phase (7.56 g/cm^3, obtained from the ICSD #9106) and Cu−8Sn−0.1P−1Ni−*x*Si alloy (8.859±0.010) g/cm^3, measured by Archimedes principle [36]), respectively. The volume fraction of $Ni_{31}Si_{12}$ phase is approximated by its area fraction. As shown in Fig. 9(a), the results indicate that the mass fraction of $Ni_{31}Si_{12}$ phase with different Ni/Si mass ratios is relatively low, fluctuating within the

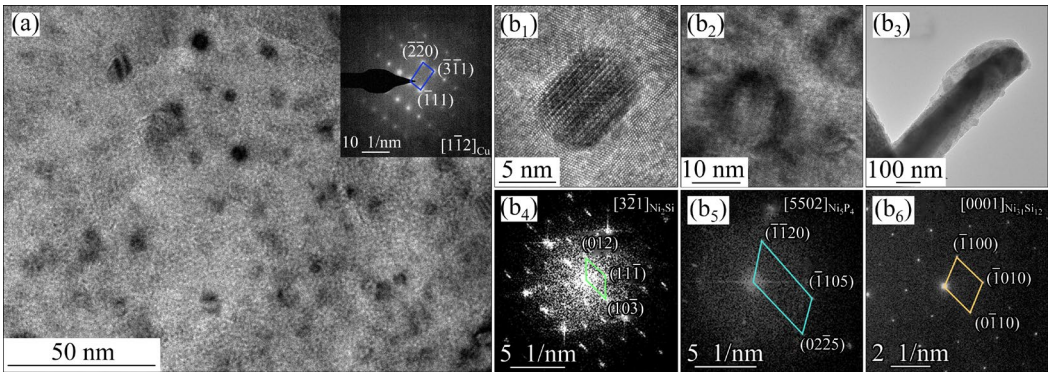

Fig. 8 TEM image of aged Cu−8Sn−0.1P−1Ni−0.227Si alloy (a), and HRTEM images of Ni_2Si (b_1, b_4), Ni_5P_4 (b_2, b_5) and $Ni_{31}Si_{12}$ (b_3, b_6) phases

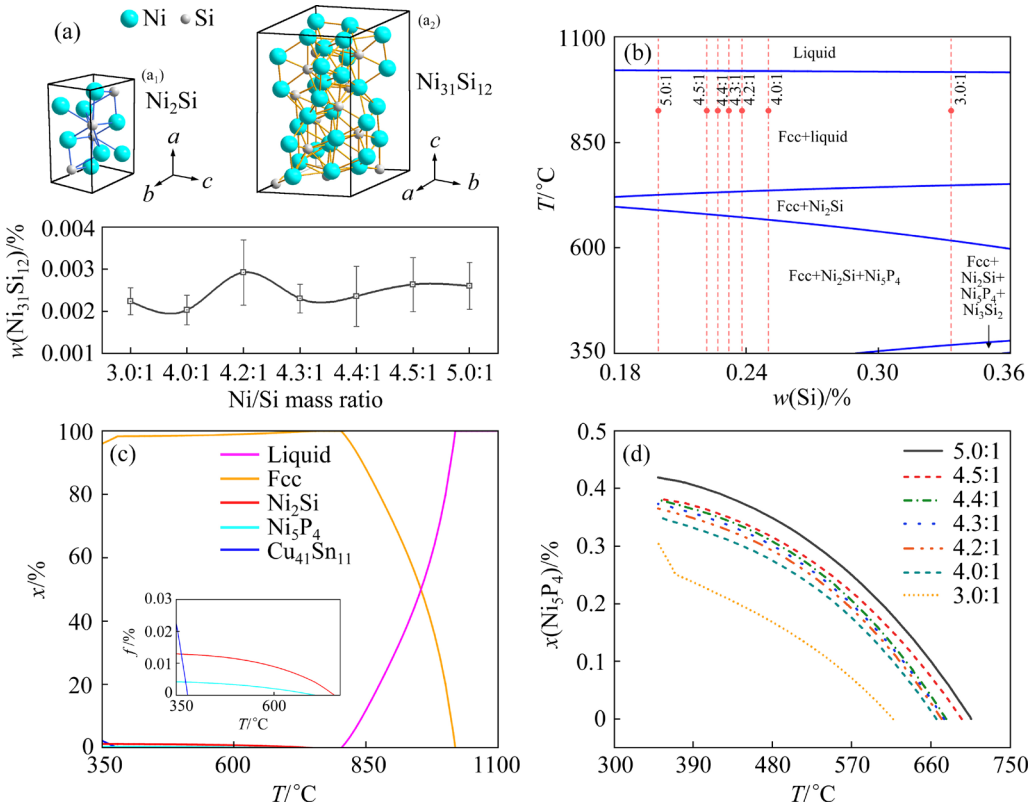

Fig. 9 (a) Mass fraction of $Ni_{31}Si_{12}$ phase with different Ni/Si mass ratios; (b) Phase diagram of Cu−8Sn−0.1P−1Ni−*x*Si alloys; (c) Phase fraction diagram of Cu−8Sn−0.1P−1Ni−0.2Si; (d) Formation curves of Ni_5P_4 phase in alloys with different Ni/Si mass ratios

range of 0.002%−0.003%. Crystal structures of Ni_2Si and $Ni_{31}Si_{12}$ unit cells are depicted in Figs. 9(a_1, a_2). Due to the Ni/Si mass ratio in the $Ni_{31}Si_{12}$ phase being greater than 2:1, the optimum Ni/Si mass ratio has undergone a change.

Additionally, the Ni_5P_4 phase forms in the Ni−Si precipitation strengthened phosphor bronze. The phase diagram of Cu−8Sn−0.1P−1Ni−*x*Si was calculated using PANDAT version 2022a and is presented in Fig. 9(b). Solidification phase transitions of the Cu−8Sn−0.1P−1Ni−*x*Si alloy with different Ni/Si mass ratios were computed at the positions of the dashed lines in Fig. 9(b). The phase transition of the Cu−8Sn−0.1P−1Ni−0.2Si alloy (Ni/Si mass ratio of 5:1) is detailed in Fig. 9(c), and the proportion of Ni_5P_4 phase is small. Furthermore, the formation curves of the Ni_5P_4 phase in alloys with different Ni/Si mass ratios were extracted, as presented in Fig. 9(d). An increasing trend in the content of the Ni_5P_4 phase is observed as the Ni/Si mass ratio increases, and the difference in Ni_5P_4 content is relatively small among alloys with Ni/Si mass ratios ranging from 4:1 to 4.5:1.

The optimal Ni/Si mass ratio of Cu−8Sn−0.1P−1Ni−*x*Si alloys is also affected by the contents of Ni and Si dissolved in the matrix. An opposing trend with the Ni/Si mass ratio is observed in the solubility of Ni and Si in the matrix, as calculated using PANDAT software (Figs. 10(a) and (b)). Figure 10(c) illustrates that, as the Ni/Si mass ratio increases, the solid solubility of Ni in the matrix is enhanced, accompanied by a decrease in the solid solubility of Si. At the intersection point, the solid solubility of Ni and Si in the matrix is low, indicating that Ni and Si can combine to form more intermetallic compounds and better strengthen the alloy. The formation of $Ni_{31}Si_{12}$ and Ni_5P_4 phases indicates that the optimal Ni/Si mass ratio for Cu−8Sn−0.1P−1Ni−*x*Si alloys is greater than 4.2:1 (atomic ratio of 2:1). Moreover, the variation trend of the solubility of Ni and Si in the matrix suggests that the optimal Ni/Si mass ratio should be in the vicinity of 4.3:1 and 4.4:1, which is consistent with the experimental results (see Figs. 3 and 4). In conclusion, due to the formation of various second phases, the Ni/Si mass ratio affects the properties of the alloy.

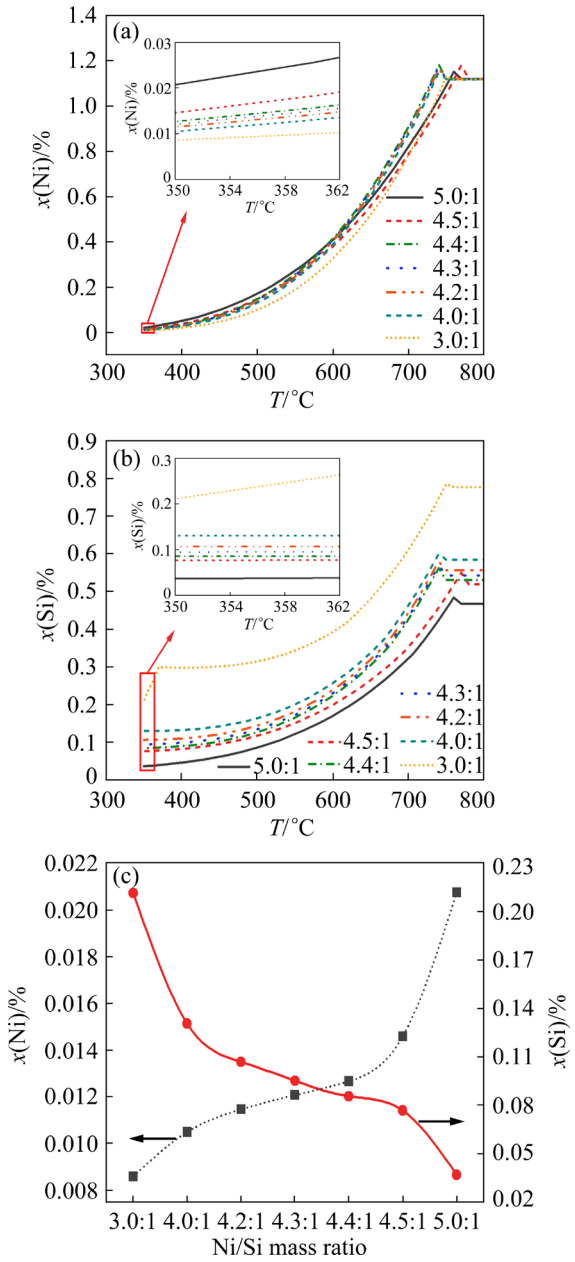

Fig. 10 Solubility variation curves of Ni (a) and Si (b) in matrix of alloys with different Ni/Si mass ratios, and trend of solid solubility of Ni and Si in matrix with respect to Ni/Si mass ratio (c)

4.2 Mechanism of brittleness in Cu−8Sn−0.1P−1Ni−0.227Si alloy after SST

The experimental results indicate that the STT temperature has a significant influence on the plasticity of the Cu−Sn−P−Ni−Si alloy. To investigate the mechanism by which the STT temperature influences plasticity, the tensile fractures of solid solution samples at 650, 700, 710, 720, 730, 740, 750, and 800 °C were characterized. The fractography shows significant changes with an

increase in STT temperature. At lower STT temperatures, the tensile fractography exhibits small and fine dimples, as shown in Fig. 11(a). This is because when the STT temperature is low, incomplete dissolution occurs, and the existing second phase leads to the formation of fine dimples [9,37]. As the STT temperature increases, the amount of the second phase dissolved into the matrix increases, and the dimple size is enlarged, as shown in Fig. 11(b). When the STT temperature rises to 710 and 720 °C, the fractography shows large and deep dimples, indicating that the solid solution effect of the alloy is significant and the plasticity is high. As the STT temperature increases further, some cracks (identified by white arrows) and quasi-cleavage fracture surfaces (identified by yellow arrows) appear on the fractography, as shown in Figs. 11(e)−(g). The transition from ductile to brittle fracture is indicated by the appearance of quasi-cleavage fracture surfaces and cracks above 730 °C. This observation is consistent with the decrease in elongation after the STT temperature exceeds 730 °C, as shown in Fig. 6. When the STT temperature reaches 800 °C, the fractography exhibits pronounced intergranular fracture, as shown in Fig. 11(h). Correspondingly, the plasticity of the alloy also becomes extremely low, and a large number of macroscopic cracks are even formed during the tensile process (see Fig. 6(a)).

When the STT temperature is too high, the reduced plasticity is caused by the formation of cracks in the Cu−8Sn−0.1P−1Ni−0.227Si alloy, and it is important to understand the reasons behind the formation of these cracks. The Cu−8Sn−0.1P−1Ni−0.227Si alloy after SST at 750 °C was characterized by energy dispersive spectroscopy (EDS), as shown in Fig. 12. The absence of significant Sn segregation at the grain boundaries in the sample after SST is revealed by EDS mapping results (see Fig. 12(c)). This finding indicates that the brittleness of the Cu−8Sn−0.1P−1Ni−0.227Si alloy is not caused by Sn segregation. After SST at 750 °C, a continuous distribution of the second phase is found at the grain boundaries of the Cu−8Sn−0.1P−1Ni−0.227Si alloy. The second phase is identified as the Ni−P phase, as shown in the EDS mapping. Due to the existence of defects such as vacancies and dislocations at grain boundaries [38,39], the atomic mobility is relatively high. In addition, the energy level at grain boundaries is high [40], leading to a preferential occurrence of nucleation and growth of new phases at grain boundaries. The difference in plasticity between the second phase at the grain boundary and the matrix is significant, and the bonding between them is weak. Therefore, cracks are easily formed during deformation, leading to the decrease in the plasticity of Cu−8Sn−0.1P−1Ni−0.227Si. As the STT temperature increases, more second phases are formed at the grain boundaries, ultimately resulting in the intergranular fracture (see Fig. 11(h)).

Through the analysis of fracture surfaces and precipitated phases, the influence of STT temperature on the microstructure and properties can be deduced. By affecting the diffusion process, the STT temperature impacts the second phase and the formation of precipitated phases along grain boundaries, thereby influencing the properties of Cu−8Sn−0.1P−1Ni−0.227Si alloy. Initially, at a lower

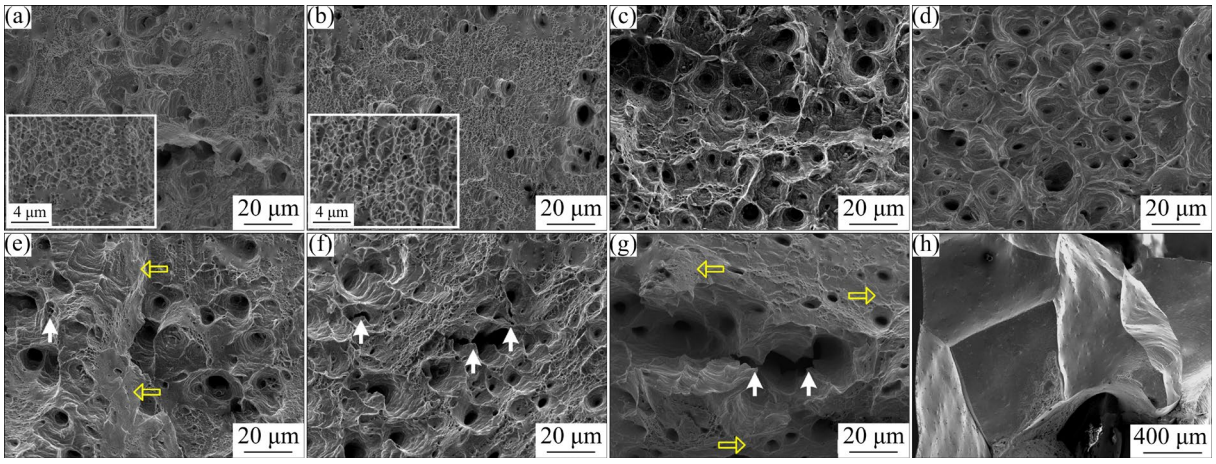

Fig. 11 Fractography of alloy at different STT temperatures: (a) 650 °C; (b) 700 °C; (c) 710 °C; (d) 720 °C; (e) 730 °C; (f) 740 °C; (g) 750 °C; (h) 800 °C

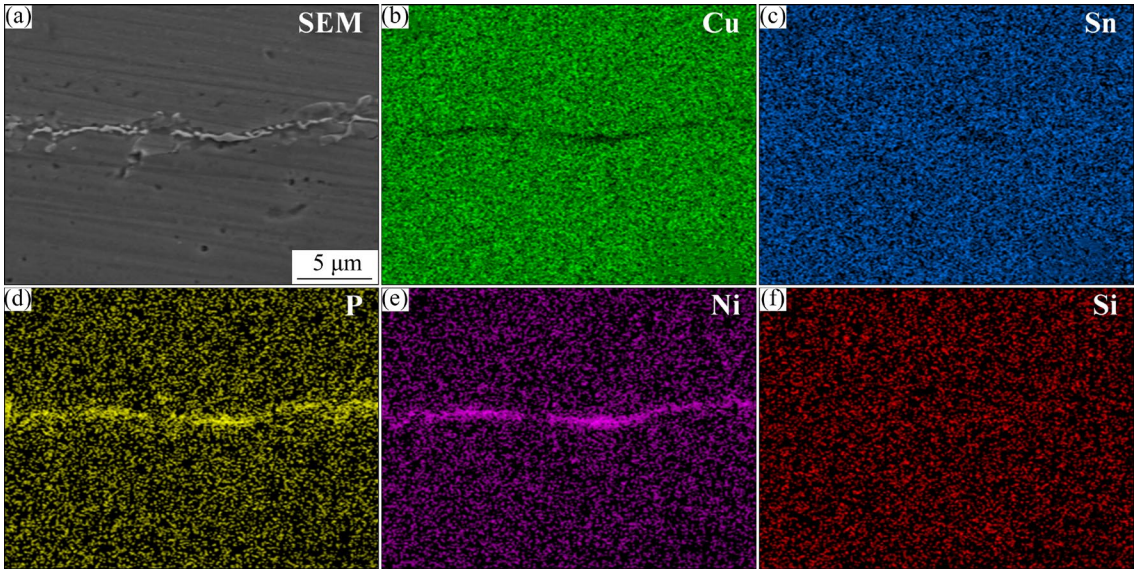

Fig. 12 EDS mapping at grain boundary of Cu−8Sn−0.1P−1Ni−0.227Si alloy solid solution treated at 750 °C for 2 h

STT temperature, the second phase cannot be adequately dissolved into the matrix in Fig. 5(a). Consequently, plasticity remains at a low level. With excessively high STT temperature, the formation of a continuous second phase at grain boundaries is promoted by the increased diffusion rate (see Fig. 12), leading to enhanced brittleness. The optimal SST temperature of the Cu−8Sn−0.1P−Z1Ni−0.227Si alloy, characterized by a well-dissolved microstructure (see Fig. 5(c)) and enhanced plasticity (see Fig. 6), is determined to be 710 °C.

From the analysis above, it can be deduced that the effect of STT temperature on the ductility of the Cu−8Sn−0.1P−1Ni−0.227Si alloy is attributed to the mechanism shown in Fig. 13. At an appropriate STT temperature, the grain boundary strength is higher, and cracks will not form at the grain boundary during the deformation process, resulting a good plasticity. At excessively high STT temperatures, the Ni−P phase forms at the grain boundaries (see Fig. 12). The Ni−P phase at the grain boundary weakly binds to the matrix [31,32], the plasticity of the second phase and the matrix also differs, and the initiation of cracks are generated during the deformation process. As the deformation continues, the propagation of cracks occurs, resulting in poor plasticity. More seriously, when the number of second phase at the grain boundary reaches a certain level, intergranular fracture will be caused. The plasticity of Cu−8Sn−0.1P−1Ni−0.227Si alloy is significantly influenced by STT temperature, and the optimal STT temperature is of great significance for the processing of Cu−8Sn−0.1P−1Ni−0.227Si alloy. According to Fig. 6, it can be observed that the elongation of the alloy is the highest at STT of 710 °C. However, the elongation begins to decrease after the STT temperature reaches 720 °C, indicating that the plasticity starts to be affected by the formation of the Ni−P phase at the grain boundaries of the Cu−8Sn−0.1P−1Ni−0.227Si alloy. Therefore, the optimal STT temperature for the Cu−8Sn−0.1P−1Ni−0.227Si alloy is 710 °C. Additionally, the mechanism of STT temperature on the plasticity of the Cu−8Sn−0.1P−1Ni−0.227Si alloy proposed in this study is also instructive for achieving hot rolling of the alloy.

4.3 Effects of aging on alloy properties

As shown in Fig. 7, the effect of aging temperature on the strength of the alloys is significant, and there is a difference in the effect on the Cu−8Sn−0.1P and Cu−8Sn−0.1P−1Ni−0.227Si alloys. To explore the underlying mechanisms, the dislocation density was calculated for the Cu−8Sn−0.1P and Cu−8Sn−0.1P−1Ni−0.227Si alloys cold-rolled to 80% and aged at different temperatures, as shown in Fig. 14(a). The dislocation density was determined via X-ray analysis based on Eqs. (2) and (3) [41,42]:

$$\beta\cos\theta_{hkl}=\frac{K\lambda}{d}+4\varepsilon\sin\theta_{hkl} \tag{2}$$

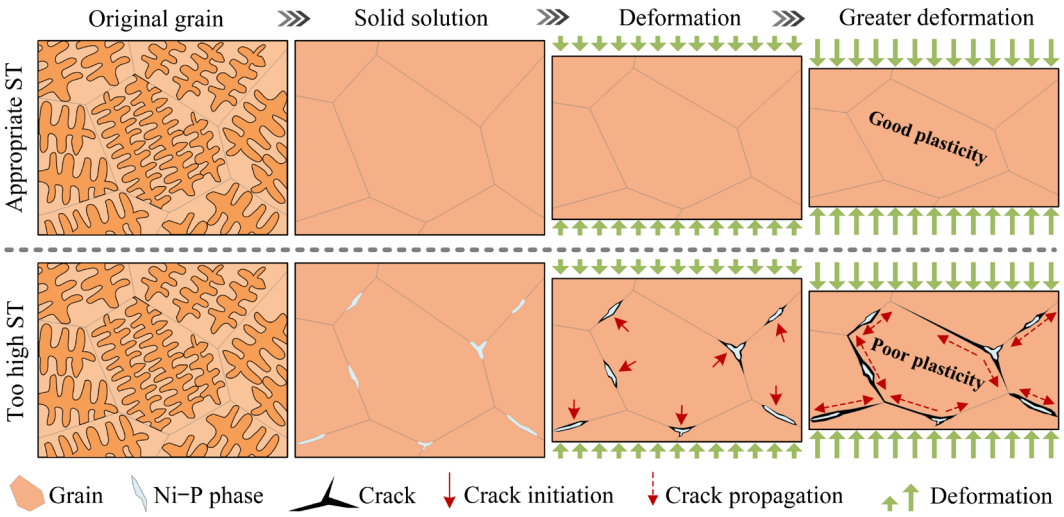

Fig. 13 Effect of STT temperature on ductility of Cu−8Sn−0.1P−1Ni−0.227Si alloy

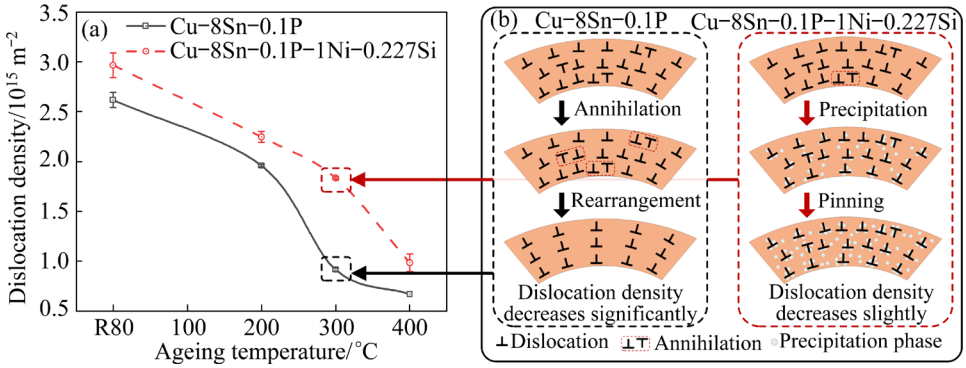

Fig. 14 (a) Dislocation density of Cu−8Sn−0.1P and Cu−8Sn−0.1P−1Ni−0.227Si alloys cold-rolled to 80% and after aging at different temperatures; (b) Mechanism of interaction between precipitation phase and dislocation motion during aging process

where β is the true full width at half maximum (FWHM), λ is the wavelength of Cu K_α radiation (λ=0.154 nm), K is a constant equal to ~0.9, θ_{hkl} is the Bragg angle, and d is the crystallite size.

$$\rho = 16.1(\varepsilon/b)^2 \tag{3}$$

where b is the magnitude of Burgers vector, ε is the micro-strain of the samples, and ρ is the dislocation density. According to Eq. (2), the parameters of $\beta\cos(\theta_{hkl})$ and $\sin(\theta_{hkl})$ are linearly dependent, and the microstrain ε can be obtained from their slopes. Then, based on Eq. (3), the dislocation density of the alloys can be calculated [43]. The dislocation density of both the Cu−8Sn−0.1P and Cu−8Sn−0.1P−1Ni−0.227Si alloys show a decreasing trend after aging at 200 °C. However, the difference is that the dislocation density of the Cu−8Sn−0.1P alloy decreases rapidly after aging at 300 °C, while the dislocation density of the Cu−8Sn−0.1P−1Ni−0.227Si alloy does not decrease significantly until aging at 400 °C. The change in dislocation density coincides with the change in strength, as shown in Fig. 7. The difference in the properties of the Cu−8Sn−0.1P and Cu−8Sn−0.1P−1Ni−0.227Si alloys during the aging process can be summarized in two aspects. One is the difference in the change of dislocation density, and the other is the difference in recrystallization behavior of the alloys. During the aging process of the Cu−8Sn−0.1P alloy, with the occurrence of recovery, dislocations begin to glide, and even annihilate and rearrange [44,45], resulting in a significant decrease in dislocation density. In copper alloys, dislocation glide and annihilation will occur at relatively low temperatures, even at room temperature [44]. For the Cu−8Sn−0.1P−1Ni−0.227Si alloy, the glide of dislocations is impeded by the precipitation of nano-sized precipitates during the aging process,

thereby mitigating the decline of dislocation density. Ultimately, a slight decrease in dislocation density is shown after aging at 300 °C. With a further increase in aging temperature, the motion of dislocations is promoted, resulting in a significant decrease in dislocation density of the Cu−8Sn−0.1P−1Ni−0.227Si alloy after aging at 400 °C. The mechanism of the interaction between the precipitation phase and dislocation motion is shown in Fig. 14(b). Besides, due to the low melting point of Cu−8Sn−0.1P and Cu−8Sn−0.1P−1Ni−0.227Si alloys (about 1025 °C), recrystallization will occur during aging at 300 °C. Nano-sized second phase precipitated in Cu−8Sn−0.1P−1Ni−0.227Si alloy during aging, which can pin grain boundaries and impede grain growth [46], thus provides higher strength. The aging temperature influences the formation of precipitated phases, and maintaining an appropriate aging temperature (300 °C) is crucial to prevent the softening of the matrix.

5 Conclusions

(1) The properties of Cu−8Sn−0.1P−1Ni−*x*Si are influenced by the Ni/Si mass ratio, attributed to the formation of various second phases. The optimum Ni/Si mass ratio is determined as 4.4:1, corresponding to the optimal alloy composition of Cu−8Sn−0.1P−1Ni−0.227Si.

(2) By influencing the diffusion process, the second phase and the formation of precipitated phases along grain boundaries are affected by STT temperature. Thereby, the properties of Cu−8Sn−0.1P−1Ni−0.227Si alloy are influenced by STT temperature, and the optimal STT temperature of Cu−8Sn−0.1P−1Ni−0.227Si alloy is determined to be 710 °C.

(3) During the aging process, the decline of dislocation density can be alleviated in the Cu−8Sn−0.1P−1Ni−0.227Si alloy due to the formation of precipitates. The excellent performance, including UTS of 866 MPa, YS of 772 MPa, and EL of 8.7%, can be achieved through 80% cold rolling deformation followed by aging at 300 °C for 4 h.

CRediT authorship contribution statement

Guo-liang LI: Conceptualization, Data curation, Methodology, Investigation, Writing − Original draft; **Zi-di HANG** and **Shi-peng YUE:** Methodology, Investigation; **Zhong-kai GUO:** Writing − Review & editing, Methodology; **Jin-chuan JIE:** Writing − Review & editing, Formal analysis, Supervision; **Ting-ju LI:** Resources, Supervision.

Declaration of competing interest

The authors declare that they have no known competing financial interests or personal relationships that could have appeared to influence the work reported in this paper.

Acknowledgments

The authors gratefully acknowledge the support of the National Key Research and Development Program of China (No. 2018YFE0306103), the National Natural Science Foundation of China (No. 52071050), and the Science and Technology Innovation Project of Ningbo, China (No. 2021Z032).

References

[1] KOHLER F, CAMPANELLA T, NAKANISHI S, RAPPAZ M. Application of single pan thermal analysis to Cu−Sn peritectic alloys [J]. Acta Materialia, 2008, 56: 1519−1528.

[2] OUYANG Jin-dong, CHEN Ming-he, WANG Ning, ZHANG Qin-chai, WANG Hui. Size effects on deformation behavior of C5210 phosphor bronze thin sheet [J]. Transactions of Nonferrous Metals Society of China, 2015, 25: 1114−1121.

[3] NAKAMACHI E, HONDA T, KURAMAE H, MORITA Y, OHATA T, MORIMOTO H. Two-scale finite element analyses for bendability and springback evaluation based on crystallographic homogenization method [J]. International Journal of Mechanical Sciences, 2014, 80: 109−121.

[4] LUO Cheng-sheng, SU Long-shui, WANG Chen, TONG Chang-qing, ZHOU Jian-hui, WANG Bing-shu, CHEN Jun-feng. Corrosion behavior of tin-phosphor bronze strips in environments containing Cl^- and HCO_3^- [J]. Materials and Corrosion, 2022, 73: 1110−1120.

[5] SO S M, KIM K Y, LEE S J, YU Y J, LIM H A, OH M S. Effects of Sn content and hot deformation on microstructure and mechanical properties of binary high Sn content Cu−Sn alloys [J]. Materials Science and Engineering: A, 2020, 796: 140054.

[6] ZHAI W, WANG W L, GENG D L, WEI B. A DSC analysis of thermodynamic properties and solidification characteristics for binary Cu−Sn alloys [J]. Acta Materialia, 2012, 60: 6518−6527.

[7] BUGGY M, CONLON C. Material selection in the design of electrical connectors [J]. Journal of Materials Processing Technology, 2004, 153: 213−218.

[8] HU Dao-chun, CHEN Ming-he, WANG Lei, WANG Hong-jun. Microstructural characterization of blanked surface of C5191 phosphor bronze sheet under ultra-high-speed blanking [J]. Transactions of Nonferrous Metals Society of China, 2021, 31: 692−702.

[9] LI Guo-liang, HANG Zi-di, YUE Shi-peng, LIU Qing, GUO Zhong-kai, DING Hai-min, JIE Jin-chuan, LI Ting-ju. Microstructures and properties of Ni−Si precipitation strengthened phosphor bronze [J]. Journal of Alloys and Compounds, 2023, 946: 169388.

[10] WANG Qiu-ping, ZHOU Rong-feng, GUAN Jie-ren, WANG Chun-jian. The deformation compatibility and recrystallisation behaviour of the alloy CuSn10P1 [J]. Materials Characterization, 2021, 174: 110940.

[11] PARK J S, PARK C W, LEE K J. Implication of peritectic composition in historical high-tin bronze metallurgy [J]. Materials Characterization, 2009, 60: 1268−1275.

[12] CAO Yi-cheng, HAN S Z, CHOI E A, AHN J H, MI Xu-jun, LEE S N, SHIN H, KIM S, LEE J. Effect of inclusion on strength and conductivity of Cu−Ni−Si alloys with discontinuous precipitation [J]. Journal of Alloys and Compounds, 2020, 843: 156006.

[13] LI Guo-dong, SHEN Yan-bai, ZHAO Si-kai, BAI Jin-zhou, GAO Shu-ling, LIU Wen-bao, WEI De-zhou, MENG Dan, SAN Xiao-guang. Construction of rGO-SnO_2 heterojunction for enhanced hydrogen detection [J]. Applied Surface Science, 2022, 585: 152623.

[14] AHN J H, HAN S Z, CHOI E A, LEE H, LIM S H, LEE J, KIM K, HWANG N M, HAN H N. The effect of bimodal structure with nanofibers and normal precipitates on the mechanical and electrical properties of CuNiSi alloy [J]. Materials Characterization, 2020, 170: 110642.

[15] YANG Hai-te, WANG Wen-wei-jiao, WANG Chen, WANG Jian, ZHOU Jian-hui, TONG Chang-qing, CHEN Jun-feng, WANG Bing-shu. Effects of aging process on properties and precipitation kinetics of Cu−Cr−Zr alloy strips [J]. Transactions of Nonferrous Metals Society of China, 2023, 33: 2439−2448.

[16] SUZUKI S, SHIBUTANI N, MIMURA K, ISSHIKI M, WASEDA Y. Improvement in strength and electrical conductivity of Cu−Ni−Si alloys by aging and cold rolling [J]. Journal of Alloys and Compounds, 2006, 417: 116−120.

[17] LI Dong-mei, WANG Qing, JIANG Bei-bei, LI Xiao-na, ZHOU Wen-long, DONG Chuang, WANG Hua, CHEN Qing-xiang. Minor-alloyed Cu−Ni−Si alloys with high hardness and electric conductivity designed by a cluster formula approach [J]. Progress in Natural Science: Materials International, 2017, 27: 467−473.

[18] LIU Gang, SUN Jun, NAN Ce-wen, CHEN Kang-hua. Experiment and multiscale modeling of the coupled influence of constituents and precipitates on the ductile fracture of heat-treatable aluminum alloys [J]. Acta Materialia, 2005, 53: 3459−3468.

[19] HAN N M, ZHANG X M, LIU S D, HE D G, ZHANG Rong. Effect of solution treatment on the strength and fracture toughness of aluminum alloy 7050 [J]. Journal of Alloys and Compounds, 2011, 509: 4138−4145.

[20] KANG Lei, ZHAO Gang, WANG Guang-dong, LIU Kun, TIAN Ni. Effect of different quenching processes following solid-solution treatment on properties and precipitation behaviors of 7050 alloy [J]. Transactions of Nonferrous Metals Society of China, 2018, 28: 2162−2172.

[21] SOKOLOWSKI J H, DJURDJEVIC M B, KIERKUS C A, NORTHWOOD D O. Improvement of 319 aluminum alloy casting durability by high temperature solution treatment [J]. Journal of Materials Processing Technology, 2001, 109: 174−180.

[22] TODA H, NISHIMURA T, UESUGI K, SUZUKI Y, KOBAYASHI M. Influence of high-temperature solution treatments on mechanical properties of an Al−Si−Cu aluminum alloy [J]. Acta Materialia, 2010, 58: 2014−2025.

[23] HEGDE S R, KEARSEY R M, BEDDOES J C. Designing homogenization–solution heat treatments for single crystal superalloys [J]. Materials Science and Engineering: A, 2010, 527: 5528−5538.

[24] ZHANG Yan-bin, LIU Lin, HUANG Tai-wen, YUE Quan-zhao, SUN De-jian, ZHANG Jun, YANG Wen-chao, SU Hai-jun, FU Heng-zhi. Investigation on a ramp solution heat treatment for a third generation nickel-based single crystal superalloy [J]. Journal of Alloys and Compounds, 2017, 723: 922−929.

[25] ZENG Cong-yuan, ZHANG Bin, ETTEFAGH A H, WEN Hao, YAO Hong, MENG W J, GUO Sheng-min. Mechanical, thermal, and corrosion properties of Cu−10Sn alloy prepared by laser-powder-bed-fusion additive manufacturing [J]. Additive Manufacturing, 2020, 35: 101411.

[26] YANG Peng, GUO Xing-ye, HE Ding-yong, SHAO Wei, TAN Zhen, FU Han-guang, ZHOU Zhen-lu, ZHANG Xiao-ya. Microstructure twinning and mechanical properties of laser melted Cu−10Sn alloy for high strength and plasticity [J]. Journal of Materials Engineering and Performance, 2022, 31: 2624−2632.

[27] YAN Li-zhen, ZHANG Yong-an, XIONG Bai-qing, LI Xi-wu, LI Zhi-hui, LIU Hong-wei, HUANG Shu-hui, ZHAO Gang. Mechanical properties, microstructure and surface quality of Al−1.2Mg−0.6Si−0.2Cu alloy after solution heat treatment [J]. Rare Metals, 2017, 36: 550−555.

[28] LI Rui-di, YUAN Tie-chui, LIU Xiao-jun, ZHOU Ke-chao. Enhanced atomic diffusion of Fe−Al diffusion couple during spark plasma sintering [J]. Scripta Materialia, 2016, 110: 105−108.

[29] LIU X Y, KANE W, MCMAHON C J. On the suppression of dynamic embrittlement in Cu−8wt.%Sn by an addition of zirconium [J]. Scripta Materialia, 2004, 50: 673−677.

[30] SHIN H S, HAN S Z, CHOI E A, AHN J H, KIM S, LEE J. Co and Ti effect on hot workability of phosphor bronze [J]. Journal of Alloys and Compounds, 2022, 903: 163778.

[31] WANG Tong-min, ZHAO Yu-fei, CHEN Zong-ning, ZHENG Yuan-ping, KANG Hui-jun. The bimodal effect of La on the microstructures and mechanical properties of in-situ A356−TiB_2 composites [J]. Materials and Design, 2015, 85: 724−732.

[32] TSZENG T C. The effects of particle clustering on the mechanical behavior of particle reinforced composites [J]. Composites Part B: Engineering, 1998, 29: 299−308.

[33] HAN S Z, CHOI E A, LIM S H, KIM S, LEE J. Alloy design strategies to increase strength and its trade-offs together [J]. Progress in Materials Science, 2021, 117: 100720.

[34] LIU Xin-yu, THAM D, YATES D, MCMAHON C J. Evidence for the intergranular segregation of tin to grain boundaries of a Cu−Sn alloy and its consequences for dynamic embrittlement [J]. Materials Science and Engineering: A, 2007, 458: 123−125.

[35] HUANG Wei-jiu, CHAI Lin-jiang, LI Zhi-jun, YANG Xu-sheng, GUO Ning, SONG Bo. Evolution of microstructure and grain boundary character distribution of a tin bronze annealed at different temperatures [J]. Materials Characterization, 2016, 114: 204−210.

[36] LIU Jia-ming, ZHANG Yu-bo, WANG Wei, LIU Shi-chao, ZHANG Jun-jia, FU Ying, WANG Tong-min, LI Ting-ju. Effects of interfacial diffusion induced infiltration process on the microstructure evolution and interfacial enhancement of CF/Mg composites [J]. Journal of Materials Processing Technology, 2021, 294: 117143.

[37] CHEN Kai-xuan, ZHANG Jia-wei, CHEN Ya-jun, CHEN Xiao-hua, WANG Zi-dong, SANDSTRÖM R. Slow strain rate tensile tests on notched specimens of as-cast pure Cu and Cu−Fe−Co alloys [J]. Journal of Alloys and Compounds, 2020, 822: 153647.

[38] KIRCHHEIM R. Reducing grain boundary, dislocation line and vacancy formation energies by solute segregation. I. Theoretical background [J]. Acta Materialia, 2007, 55: 5129−5138.

[39] van HELENA S. Grain boundaries and dislocations [J]. Science, 2002, 296: 66−67.

[40] LI Lin-lin, KAMACHALI R D, LI Zhi-ming, ZHANG Zhe-feng. Grain boundary energy effect on grain boundary segregation in an equiatomic high-entropy alloy [J]. Physical Review Materials, 2020, 4: 053603.

[41] ZHANG Y, TAO N R, LU K. Mechanical properties and rolling behaviors of nano-grained copper with embedded nano-twin bundles [J]. Acta Materialia, 2008, 56: 2429−2440.

[42] YU Cun, AOUN B, CUI Li-shan, LIU Yi-nong, YANG Hong, JIANG Xiao-hua, CAI Song, JIANG Da-qiang, LIU Zun-ping, BROWN D E, REN Yang. Synchrotron high energy X-ray diffraction study of microstructure evolution of severely cold drawn NiTi wire during annealing [J]. Acta Materialia, 2016, 115: 35−44.

[43] GUO Zhong-kai, JIE Jin-chuan, LIU Jia-ming, YUE Shi-peng, LIU Shi-chao, LI Ting-ju. Effect of cold rolling on aging precipitation behavior and mechanical properties of Cu−15Ni−8Sn alloy [J]. Journal of Alloys and Compounds, 2020, 848: 156275.

[44] KUO Chen-ming, LIN Chih-sheng. Static recovery activation energy of pure copper at room temperature [J]. Scripta Materialia, 2007, 57: 667−670.

[45] KOHNERT A A, CAPOLUNGO L. The kinetics of static recovery by dislocation climb [J]. NPJ Computational Materials, 2022, 8: 104.

[46] ZHU Kai, YANG Zhen-guo. Effect of magnesium on the austenite grain growth of the heat-affected zone in low-carbon high-strength steels [J]. Metallurgical and Materials Transactions A: Physical Metallurgy and Materials Science, 2011, 42: 2207−2213.

通过成分和热处理工艺优化提升 Cu−Sn−P−Ni−Si 合金的综合性能

李国梁[1]，杭子迪[1]，岳世鹏[1]，郭中凯[2]，接金川[1,3]，李廷举[1,3]

1. 大连理工大学 材料科学与工程学院 辽宁省凝固控制与数字化制备技术重点实验室，大连 116024；
2. 枣庄学院 光电工程学院，枣庄 277160；
3. 大连理工大学 宁波研究院，宁波 315000

摘　要：为了优化 Ni−Si 析出强化锡磷青铜的综合性能，探究了 Ni/Si 质量比和热处理工艺对 Cu−8Sn−0.1P−1Ni−*x*Si 合金的影响。采用高分辨率场发射扫描电镜和透射电镜进行显微组织表征。结果表明，由于多种第二相形成使得合金性能受 Ni/Si 质量比的影响。同时，通过影响扩散速率，固溶处理影响了合金的显微组织和性能。通过影响位错的运动，时效过程中析出的纳米相提升了合金的强度。最终，Cu−8Sn−0.1P−1Ni−0.227Si 合金获得了优异的综合性能，其抗拉强度、屈服强度和伸长率分别为 866 MPa、772 MPa 和 8.7%。

关键词：锡磷青铜；Ni/Si 质量比；析出；固溶；Cu−Sn−P−Ni−Si 合金

(Edited by Xiang-qun LI)